Investigation of a Francis turbine during speed variation: Inception of cavitation

Chirag Trivedi [a, *], Igor Iliev [a], Ole Gunnar Dahlhaug [a], Zoran Markov [b], Fredrik Engstrom [c, d], Henning Lysaker [e]

[a] *Waterpower laboratory, NTNU—Norwegian University of Science and Technology, Trondheim 7491, Norway*
[b] *Faculty of Mechanical Engineering, Ss. Cyril and Methodius University, Skopje, 1000, Macedonia*
[c] *Vattenfall AB, Aurorum 12, Luleå, 971 77, Sweden*
[d] *Division of Fluid and Experimental Mechanics, Luleå University of Technology, Luleå, 971 87, Sweden*
[e] *Rainpower Norge AS, S. P. Andersens Veg 7, Trondheim, 7031, Norway*

ARTICLE INFO

ABSTRACT

Variable-speed operation of a hydro turbine is considered as an alternative option to meet fluctuating energy demand as it allows high-ramping rate. Cavitation can be a limiting factor to utilize the variable-speed technology at full potential in a hydro power plant. This work investigates the cavitation characteristics and unsteady pressure fluctuations as turbine ramps up, to meet the energy demand. The investigated Francis turbine consists of 15 blades and 15 splitters, and the reference diameter is 0.349 m. Numerical model of complete turbine is prepared and hexahedral mesh is created. Rayleigh Plesset algorithm is activated for cavitation modelling. Available experimental data of model acceptance test are used to prescribe boundary conditions, and to validate the numerical results at distinct points. Transient behaviour of the cavitation is studied, and the results are quite interesting. At certain time instants, the cavitation effect is extremely predominant, and as a result of cavitation bubble bursts, the amplitudes of pressure fluctuations are significantly high.

1. Introduction

On demand energy market and favourable policies to encourage the usage of renewable energy have led to continuous increase of grid connected wind, solar, and other power in recent years. Penetration of intermittent energy above the manageable limit has induced unstable grid operations. On the other hand, the consumers more − or − less expect to be able to draw greater or lesser amount of grid power, whensoever require, at their discretion, and they expect the grid to accommodate this flexibility. Flexibility of power generation is an important requirement for futuristic turbine designs. The turbines need to operate outside the guaranteed region with frequent start-stop and ramping. The power generation at off-design load brings certain challenges, such as high-amplitude pressure pulsations, vortex breakdown, cavitation, resonance and damage from rotor-stator interactions [1—3]. Variable-speed operation of hydro turbines is seen as an alternative solution to achieve

high ramping rate [4]. In case of synchronous-speed turbine, rotational speed of the runner is fixed and the turbine is operated along the line of synchronous speed. The power output is managed by guide vane opening. For variable-speed operation, two parameters, i.e., flow rate through guide vanes and rotational speed of the runner, can be used to operate the turbine optimally. To achieve speed variation, additional electronics are required, which allow continuous operation and the frequency controller that convert input frequency to 50 Hz output before injecting power to the transmission line. By adjusting the rotational speed and the flow rate, consequences related to vortex breakdown, resonance and dynamic loading can be reduced [5,6]. The efficiency at off-design conditions can be improved [4]. Cavitation is one of critical problems as it causes erosion, efficiency drop and limits the turbine operation [7—9].

Thermodynamic phase of a liquid is dependent on the pressure and temperature. Tensile stress between the molecules of liquid changes as pressure/temperature changes. When the tensile stress is larger than the bounding force, the molecules break apart and the liquid will *rupture* into gaseous phase to form a cavern, a

Nomenclatures

C	Chord (m)
$\tilde{c}_p$	Coefficient of fluctuating pressure
D	Runner reference diameter (m), $D = 0.349$m
E	Specific hydraulic energy (J kg^{-1}), gH
$\hat{e}$	Uncertainty (%)
f	Frequency (Hz)
H_n	Net head (m)
l	Length (m)
n	Runner rotational speed (revolutions per minute)
n_{ED}	Speed factor, $nD/\sqrt{E}$
NPSE	Net-positive suction energy (m), $(\Delta p + p_{amb} - p_{va})/\rho_2 + v_2^2/2$
p	Pressure (Pa)
$\tilde{p}_E$	Factor of pressure fluctuations
p^*	Normalized pressure, $(p - p_{\min})/(p_{\max} - p_{\min})$
Q	Flow rate (m^3 s^{-1})
Q_{ED}	Discharge factor, $Q/D^2\sqrt{E}$
T	Torque (N m)
t	Time (s)
v	Flow velocity (m s^{-1})

v^*	Normalized velocity, $(v - v_{\min})/(v_{\max} - v_{\min})$
v_c	Characteristic velocity (m s^{-1})
z	Number of blade/guide vane
η	Efficiency
σ	Thoma number, NPSE/E
ρ	Density (kg m^{-3})
θ	Runner circumference angle (˚)
α	Guide vane angle (˚)
γ_v	Vapour volume fraction
ψ	Specific hydraulic energy coefficient
ϕ	Flow coefficient

subscript

|	
amb	Ambient
b	Blade
exp	Experimental
gv	Guide vane
M	Model
num	Numerical
pl	Plant
th	Theoretical
va	Vapour

phenomenon also referred to as cavitation [10]. The cavitation nucleation can be homogeneous and/or heterogeneous depending on local condition. For instance, in hydro turbines, largely heterogeneous nucleation is observed, where nuclei formation occurs on the no-slip wall of blades — or at the boundary between water and dissolved particles. Typical examples of cavitation types in hydro turbines are travelling bubble cavitation, bubble cavitation beneath shear layer, localized attached and detached vortex cavitation [11–13].

Cavitation on the blade leading-edge is an example of localized attached cavitation that is observed on the suction side (when the specific hydraulic energy (E) is high from the optimal value) and the pressure side (when E is low from the optimal value) of the blades. Fig. 1 shows examples of cavitation types in Francis and Kaplan turbines. Travelling bubble cavitation occurs at high load when the pressure difference on the blade is large enough and the local pressure on the suction side drops below the vapour pressure. This type of cavitation is sensitive to the content of nuclei, water quality [14] and Thoma number (σ). Boundary layer separation due to adverse pressure gradient plays critical role for inception of cavitation [15–17]. A curvature of blades connected to the crown leads to adverse pressure gradient and the flow separation that, in many cases, results in bubble cavitation beneath shear layer and the detached (inter blade) vortex cavitation [18,19]. The bubble tends to collapse/burst on the surface when pressure inside the bubble drops below the hydrodynamic pressure exerted by the fluid [20,21]. Consequently, intense noise and pressure pulse are developed, and propagate through the surrounding medium. Bubble interface attached to the blade wall tends to flatten during the collapse and a hollow is developed on the opposite face [22]. Then, a re-entrant jet sets in towards the wall, with a rapidly increasing velocity. Finally, the jet pierces into the bubble and impinges on the wall. Because of very high velocity, the re-entrant jet is often considered as a possible hydrodynamic mechanism for cavitation erosion. It is worth to note that, for each turbine, the cavitation is dependent on blade design, operating load, content of nuclei and Thoma number. Therefore, cavitation properties from-turbine-to-turbine may vary.

Cavitation characteristics (systematic variation of σ) are generally determined during model acceptance tests and the scale factor is implemented to the corresponding prototype. IEC 60193:1999 [24] provides information for cavitation tests ($\sigma_M \geq \sigma_{pl}$) and minimum requirement for similitude, especially Reynolds (Re) and Froude (Fr) numbers. Reynolds number of a model is smaller than the prototype, where the ratio of friction losses to total losses for the model becomes larger than the corresponding ratio for the prototype. As a result, the model efficiency is smaller than that of prototype. The influence of Fr is very important especially when $Fr_M \neq Fr_P$ and low specific hydraulic energy (< 100 J kg^{-1}) because of reduced measurement accuracy and risk of degassing in the low-pressure region.

Turbine cavitation has been studied by many researchers during last two decades [25–28]. The studies focused on efficiency drop at off-design conditions, erosion due to cavitation [29], nuclei formation [30], high frequency vibrations [31,32], acoustic noise [33], etc. Cavitation during transient conditions, variable-speed, ramping, start-stop, is substantially different from that of steady state conditions of the turbine or other simplified cases, i.e., hydrofoil [34–40].

The cavitation, in the runner, is dependent on local pressure along the blade length. The variable-speed operation influences the local pressure, depending on the load and the blade design. Therefore, it is quite important to study the cavitation and its aggressiveness with rotational speed. So far, cavitation research was focused on distinct operating points of the turbines under steady state conditions. However, flow during the transient conditions is accelerating/decelerating and rotating, and the relative velocity changes constantly. Very limited knowledge is available when it comes to cavitation during the transient conditions of hydro turbines. Studies [41–44] on the bubble dynamics showed that the relative velocity on the bubble interface play critical role on cavitation inception and the aggressiveness. In this work, we aim to investigate the cavitation characteristics numerically under variable-speed operation of a model Francis turbine. Numerical simulations of the existing model turbine are conducted and global parameters, such as head, efficiency, torque and power are
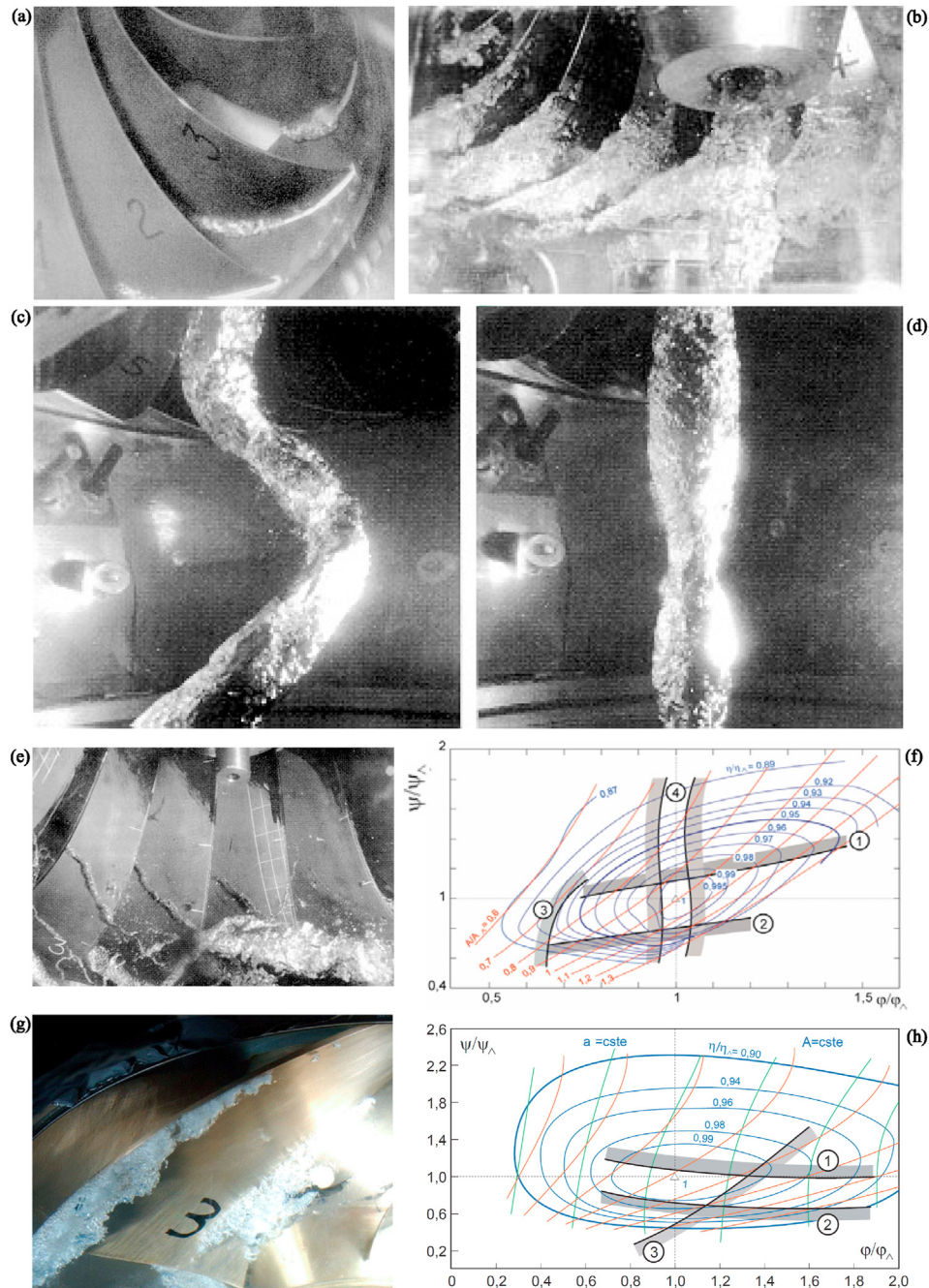
Fig. 1. Examples of cavitation types in Francis and Kaplan turbines. (a) leading edge cavitation, (b) travelling bubble cavitation, (c) cavitation vortex at part load, (d) cavitation vortex at high load, (e) inter blade cavitation vortices, (f) hill diagram of Francis turbine indicates the possible cavitation occurrence according to operating loads, 1 - leading edge suction side cavitation, 2 - Leading edge pressure cavitation, 3 - inter blade cavitation vortices, 4 - cavitation vortex at runner downstream (g), tip clearance and hub cavitation in Kaplan turbine and (h) hill diagram of Kaplan turbine indicates the possible cavitation occurrences according to operating loads, 1 - leading edge suction side cavitation, 2 - Leading edge pressure cavitation, 3 - hub cavitation [23].

validated at distinct steady state points. Then, cavitation phenomenon in the turbine (as rotational speed of the runner increases) is investigated.

2. Francis turbine

2.1. Experimental setup

The test rig is a reduced scale (1:5.1) model of a prototype Francis turbine ($N_{QE} = 0.027$ — see IEC 60193:1999 sub clause 1.3.3.12.11) operating in Norway. The model turbine includes 14 stay vanes integrated into the spiral casing, 28 guide vanes, a runner with 15 blades and 15 splitters, and a draft tube. Fig. 2 shows geometry of Francis turbine. The runner inlet and outlet diameters are 0.63 and 0.347 m, respectively. The test facility is equipped with all necessary sensors to acquire data such as pressure, flow rate, torque, water temperature and rotational speed. Detailed description about the test facility is presented in our previous publications [5,6].
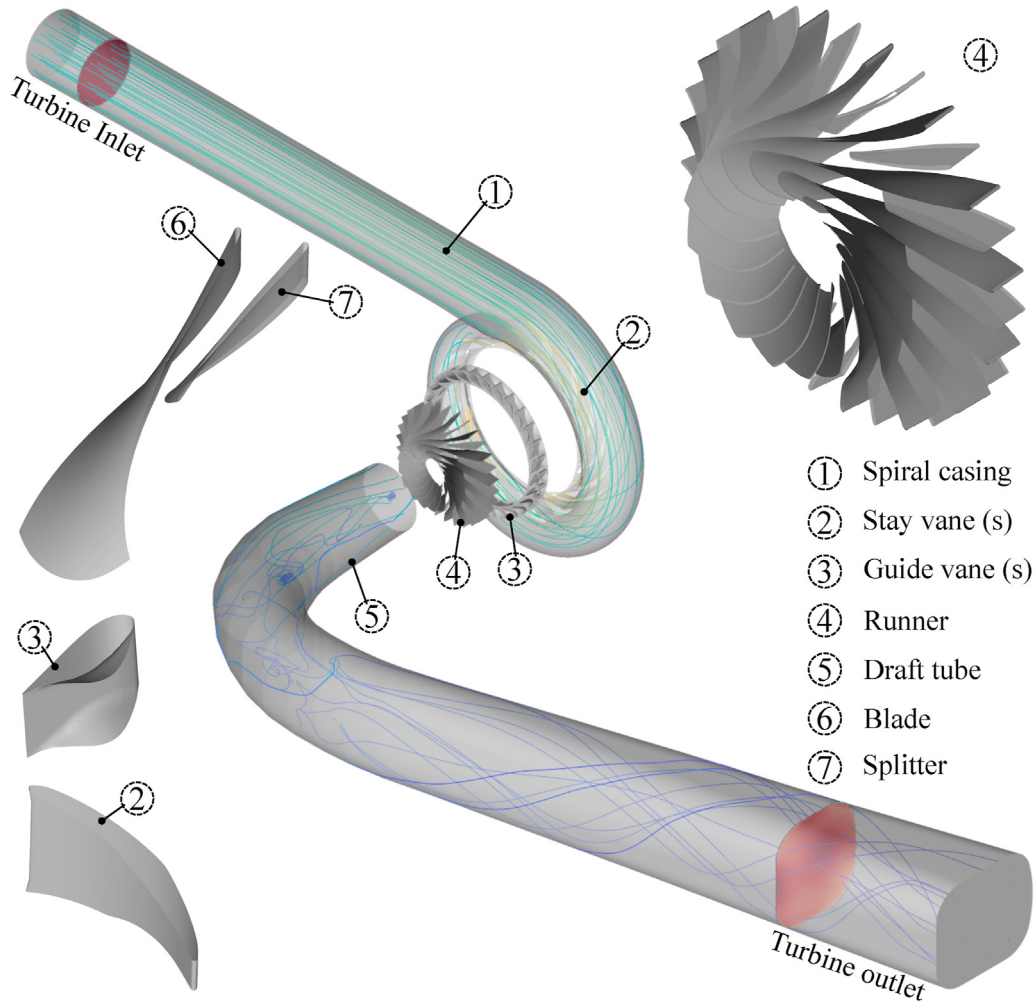
Fig. 2. Numerical model of Francis turbine prepared for the present work.

2.2. Numerical setup

The numerical model of Francis turbine consists of three domains as follows: (1) an inlet conduit, spiral casing, stay vanes and guide vanes, (2) a runner with 15 blades and 15 splitters (Fig. 3), and (3) a draft tube. A hexahedral mesh is created in all the domains, and the total number of nodes are 28 million ($0.1 \leq y^+ \leq 30$). The rotating and stationary domains are connected through an interface modeling approach, a multiple reference frame. The frozen rotor and transient rotor-stator interfaces are enabled for the steady-state and unsteady simulations, respectively. For turbulence modeling, shear stress transport model with automatic wall function was used [45]. A well proven Rayleigh−Plesset model is used for the vapour phase of cavitation [46,47]. The growth of a vapour
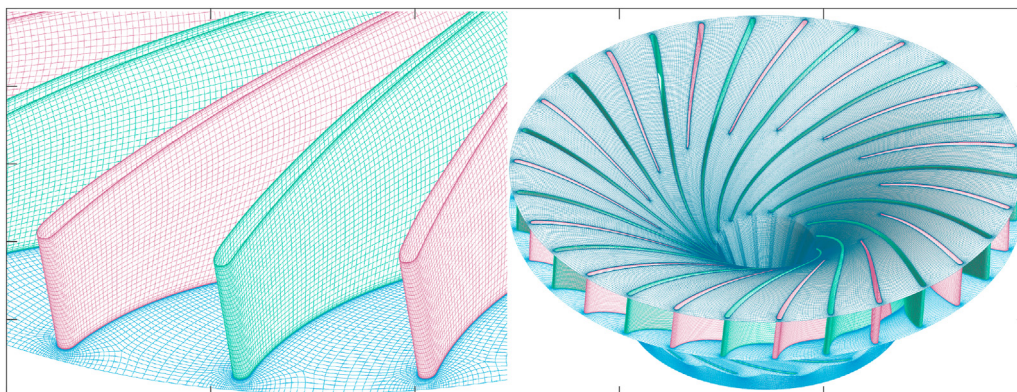

Fig. 3. Francis runner and hexahedral mesh used for the numerical simulations.

bubble in a liquid is solved by equation (1).

$$R_B \frac{d^2 R_B}{dt^2} + \frac{3}{2}\left(\frac{dR_B}{dt}\right)^2 + \frac{2\phi}{\rho_w R_B} = \frac{p_v - p}{\phi_w}, \tag{1}$$

where R_B is bubble radius in m, p_v is vapour pressure in Pa, p is pressure around a bubble in Pa, ρ_w is density of water in kg m^{-3}, ϕ is surface tension coefficient between the liquid and the vapour. Table 1 depicts the parameters used for the numerical modelling in this work.

2.3. Numerical simulations and validation

The adopted strategy was to validate the numerical model, first, at the best efficiency point then full load. If the results are satisfactory, perform simulations with cavitation and validate the model at same loads. Following sets of simulations were carried out to ensure proper conversion of solution parameters and to establish the credibility of the results.

- Steady state and unsteady simulations at the best efficiency point, $Q_{ED} = 0.15$ and $n_{ED} = 0.18$.
- Simulations with and without cavitation, $Q_{ED} = 0.23$ and $n_{ED} = 0.14$.
- Simulations with and without cavitation, $Q_{ED} = 0.17$ and $n_{ED} = 0.22$.
- Unsteady simulation of variable-speed approach with cavitation, $\alpha = 140\%$, $n_{ED} = 0.14 - 0.22$.

Fig. 4 shows the iso-efficiency hill-diagram (experimental data — model acceptance test) of the turbine. The error in hydraulic efficiency during the model acceptance tests was ± 0.19%. These experimental results are used for imposing the boundary conditions and validating the numerical model. Table 2 shows validation errors in flow rate ($\hat{e}_Q$), torque ($\hat{e}_T$) and hydraulic efficiency ($\hat{e}_\eta$). The errors were quantified using methods described in the literature [48,49]. For all simulations, the guide vane opening was maximum ($\alpha = 140\%$), except for the best efficiency point ($\alpha = 100\%$). The validation errors at the best efficiency point without cavitation ($Q_{ED} = 0.15$, $n_{ED} = 0.18$) are 1.73%, 0.58% and 1.94% in flow rate ($\hat{e}_Q$), torque ($\hat{e}_T$) and hydraulic efficiency ($\hat{e}_\eta$), respectively. The validation errors at full load with cavitation ($Q_{ED} = 0.17$, $n_{ED} = 0.22$) are 7.04%, 8.96% and 9.49% in flow rate ($\hat{e}_Q$), torque ($\hat{e}_T$) and hydraulic efficiency ($\hat{e}_\eta$), respectively. Errors at the best efficiency point are minimum, where the flow condition is stable and

Table 1
Solution parameters and the description for numerical setup.

Parameters	Description
Modelling approach	Complete turbine
Mesh type, nodes, y^+	Hexahedral, 28 million, $0.1 \leq y^+ \leq 30$
Solution approach	Steady state and Unsteady
Interface modelling	Transient rotor stator
Phase modelling	Multiphase, cavitation
Cavitation model	Rayleigh–Plesset
Vapour pressure	2307 Pa
Boundary types	Total pressure: inlet of spiral casing
	Static pressure (opening): outlet of draft tube
Advection scheme	High-resolution
Time marching scheme	Second order backward Euler
Turbulent intensity	5%
Turbulence model	Shear stress transport (automatic wall function)
Time step	1° of runner rotation
Total time	67 revolutions of runner (≈ 7. seconds)
Runner rotational speed	Variable speed, $n_{ED} = 0.18$, $531.7^{\pm 118}$ rpm

the turbine operates smoothly without cavitation. However, the errors increase with the modelling complexities and away from the design load. The maximum error in the present work is obtained at the full load, with cavitation and high rotational speed. In this turbine, the full load operation is far away, i.e., 40% overload and the rotational speed is 1.22 times the synchronous speed. The flow separation in the blade channels is predominant, and the effect of vortex breakdown is high. Numerical errors under such complex conditions are high even with the fine mesh, low y^+ and sophisticated turbulent models [48,50]. Requirement of computational resources is exponentially high and often falls outside the economic limit to resolve turbulent eddies of the order of very small scale in turbomachinery.

3. Results and discussions

Results in this section primarily focus on transient variation and inception of cavitation in the turbine as rotational speed increases from one operating condition to another. The cavitation value (Thoma number) is much smaller than the sigma plant ($\sigma_{pl} = 0.05$) in this study. Based on validation analysis (Table 2) of the prepared numerical model, final simulations of variable-speed operation were conducted — expected error is up to 10%. The user defined script (equation (2)) was implemented in the CFX® solver to perform variable-speed operation numerically.

$$\begin{aligned} &\text{if } t_0 \leq t \leq t_1, n = n_1; \\ &\text{elseif } t_1 < t < t_2, n = \frac{n_2 - n_1}{t_2 - t_1}; \\ &\text{else } t_2 \leq t \leq t_3, n = n_2; \\ &\qquad \text{end} \end{aligned} \tag{2}$$

where t_0, t_1, t_2 and t_3 are 0, 1, 6 and 7 s, respectively. Phase-I: time 0–1 s, runner spins at fixed speed, i.e., 413.5 rpm ($n_{ED} = 0.14$). Phase-II: time 1 s, the rotational speed increases linearly from 413.5 rpm to 649.7 rpm ($n_{ED} = 0.14 - 0.22$, see variable-speed line in Fig. 3). Phase-III: time 6–7 s, the runner spins fixed speed, i.e., 649.7 rpm ($n_{ED} = 0.22$). The turbine operating head was maintained, i.e., around 30 m, during the speed variation. Numerical points were created at distinct locations in the turbine to monitor cavitation and the resulting pressure amplitudes. An overall observation is that initially ($0.14 \leq n_{ED} \leq 0.20$) the cavitation is low however, during the later phase ($0.20 \leq n_{ED} \leq 0.22$), it is intensified and appeared in the entire turbine.

Fig. 5 (a) shows pressure fluctuations and the amplitudes at k_1 location of the vaneless space. The overall static pressure in the vaneless space increases gradually with the rotational speed. During 0–6 s, the fluctuations are normal and related to the rotor-stator interaction frequencies. The extended window, $t = 4 - 4.2$ s, of Fig. 5(a) depicts the fluctuations of rotor-stator interaction frequency (f_s). The amplitudes of pressure fluctuations are normalized by specific hydraulic energy (E, see IEC 6093:1999 sub clause 4.3.6.1.3).

$$f_s = nz_b (\text{Hz}), \tag{3}$$

$$\tilde{p}_E = \frac{\tilde{p}(t)}{\rho E}, \tag{4}$$

where n is the runner rotational speed in revolutions per second and z_b is the number of blades (including splitters) in a turbine, $\tilde{p}(t)$ is the time-dependent fluctuating pressure in Pa and ρ is the water density kg m^{-3}. The f_s increases from 206.7 Hz to 324.8 Hz with the rotational speed during 1–6 s. At 4.6 s, pressure in the vaneless
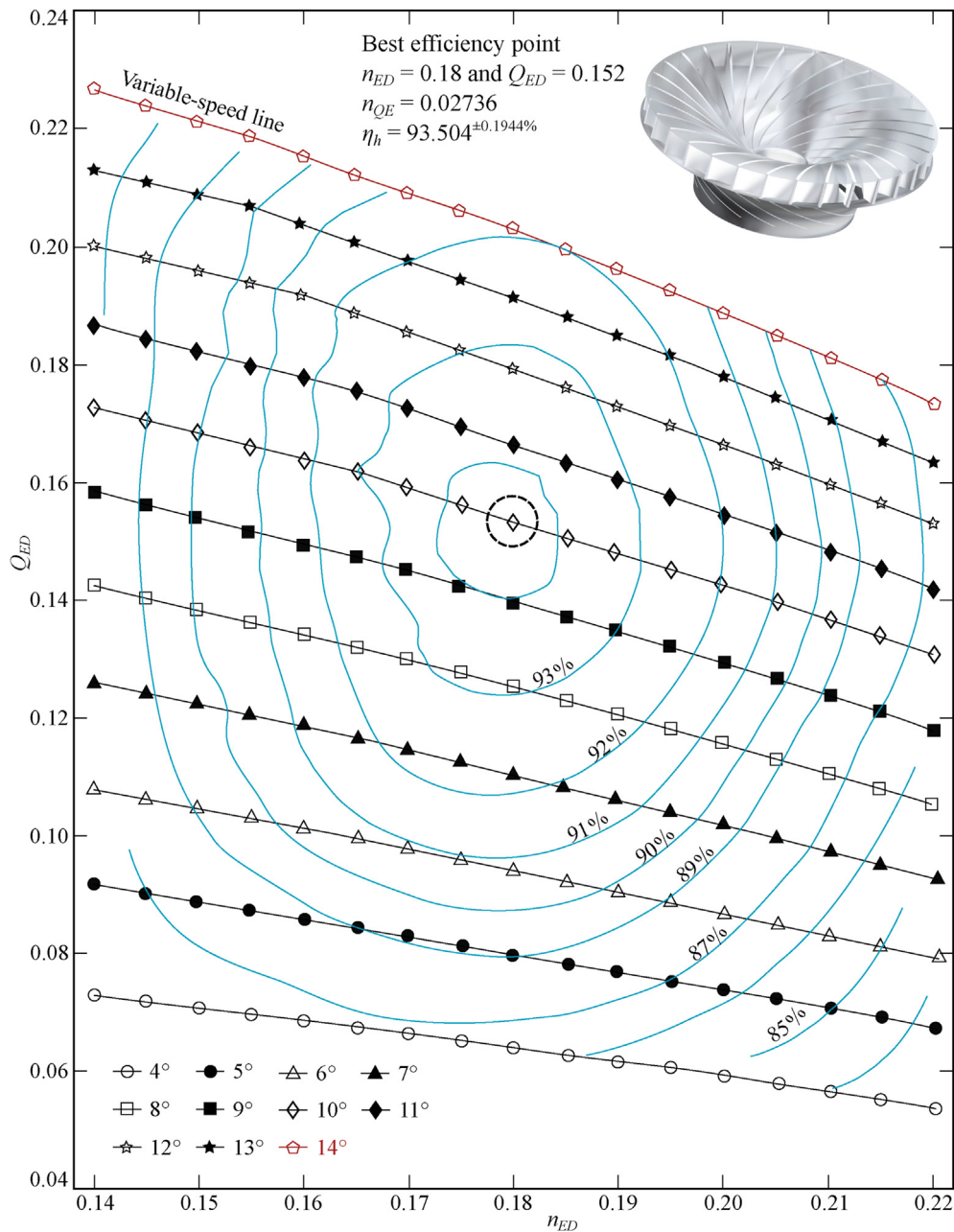
Fig. 4. Iso-efficiency hill-diagram of a model Francis turbine. Retrieved from the repository of model acceptance tests in the laboratory. Constant guide vane angle (α) of 14° shows the path of variable-speed operation of the turbine in this study.

space drops to the vapour pressure and develops a pulse of high pressure, when the cavitation bubbles spurt, and returns to the normal loading at 4.8 s. The similar cavitation effects were obtained at time instances of 5.1, 5.7, 5.8 and 6.6 s. However, at 5.8 s, intensity of cavitation was high and resulted in pulse of very high pressure, almost 20 times that of normal loading. Fig. 5(b) shows vapour volume fraction in the guide vane passages at time instant of 5.8 s, $\gamma_v = 0$ refers to vapour content. Predominant vapour content clearly indicates the strong cavitation in the large section of guide vanes. The cavitating zone is spread across the stay vane passage and a section of spiral casing. Pressure fluctuations at other locations in the vaneless space are shown in Fig. 6. Points k_1, k_2 and k_3 are in the vaneless space on the same radius from the turbine axis, and they are 120° apart from each other. Intensity of cavitation and

the time at k_2 and k_3 are slightly different from that of k_1. There was no systematic pattern on the occurrence of cavitation. The asymmetric loading on the nearby guide vane is inevitable. Fig. 7 shows comparison of pressure loading on a guide vane during non-cavitating and cavitating conditions. The pressure loading ($\tilde{c}_p$) is extracted on the mid-span of the guide vane (near to k_1). Pressure at the leading edge ($l/c = 0$) is close to vapour pressure, which increases and drops suddenly again as flow velocity in the passage increases. Two fulcrum points of $\tilde{c}_p$ exhibit, where the loading switches from pressure to suction side at 7% chord length and vice versa at 35% chord length. Furthermore, sharp change in loading at the trailing edge can be seen.
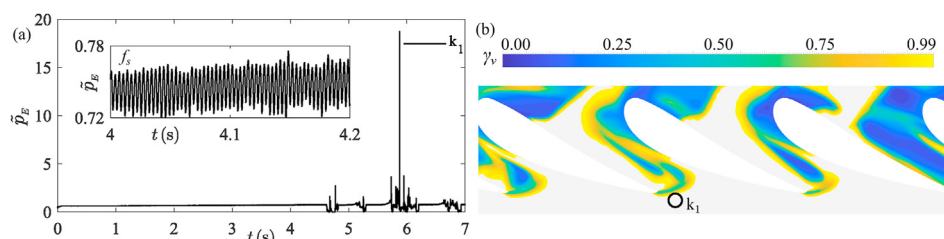
Table 2
Solution approaches and validation error, $(\hat{e}_{exp} - \hat{e}_{num})/\hat{e}_{exp}$.

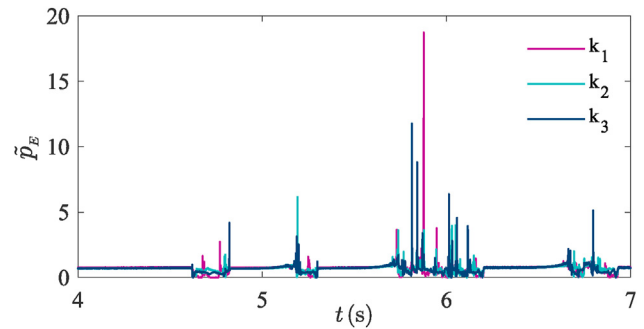| Solution	Turbine operating point	Error (%)		
		$\hat{e}_Q$	$\hat{e}_T$	$\hat{e}_\eta$
1	Best efficiency point, steady state, $Q_{ED} = 0.15, n_{ED} = 0.18, \alpha = 100\%$	1.73	0.58	1.94
2	Best efficiency point, Unsteady, $Q_{ED} = 0.15, n_{ED} = 0.18, \alpha = 100\%$	1.52	0.46	1.63
3	Steady state, $Q_{ED} = 0.23, n_{ED} = 0.14, \alpha = 140\%$	2.06	3.98	4.28
4	Steady state, cavitation, $Q_{ED} = 0.23, n_{ED} = 0.14, \alpha = 140\%$	2.41	4.15	4.35
5	Unsteady, cavitation, $Q_{ED} = 0.23, n_{ED} = 0.14, \alpha = 140\%$	2.16	5.01	5.27
6	Steady state, $Q_{ED} = 0.17, n_{ED} = 0.22, \alpha = 140\%$	5.81	8.37	9.31
7	Steady state, cavitation, $Q_{ED} = 0.17, n_{ED} = 0.22, \alpha = 140\%$	6.73	9.20	9.51
8	Unsteady, cavitation, $Q_{ED} = 0.17, n_{ED} = 0.22, \alpha = 140\%$	7.04	8.96	9.49

$$\tilde{c}_p = \frac{p - \overline{p}}{\rho E}, \tag{5}$$

where p is the static pressure in Pa and $\overline{p}$ is an average pressure across the guide vane chord length at same time instant in Pa, E is the specific hydraulic energy in J kg^{-1}. Fig. 8 shows pressure contour, $\tilde{c}_p$, on mid-span of stay vane and guide vane channels at $t = 5.8$ s, i.e., when the cavitation is intense. Asymmetric distribution of pressure can be seen. The low pressure region is from $\theta = 90°$ to $270°$ of circumference, guide vane channels $15 - 28$, and the spot of intense cavitation is around guide vane #20. The enlarged window of guide vane #20 shows the pressure contours, $\tilde{c}_p$, superimposed by streamlines. Strong recirculation on the cavitation spot is visible. Four distinct zones of cavitation are formed locally in this guide vane and stay vane channel. The cavitation spot was slowly moved towards the runner through vaneless space as simulation advanced. Flow field in the vaneless space is more complex than the guide vane and stay vane channels. Circumferential velocity due to runner rotation is predominant in the vaneless space. Large part of the potential energy is converted to the kinetic energy once the flow leaves the guide vane channels, and the components of circumferential and relative velocities become predominant. Pressure field from the guide vane trailing edge and the blade leading edge interact, and creates complex cyclic pattern. Variation in the pressure field is dependent on the instantaneous blade position relative to the guide vane trailing edge. Detailed investigations on the pressure field in the vaneless space and how flow field changes with blade's angular position are presented in our previous work [51].
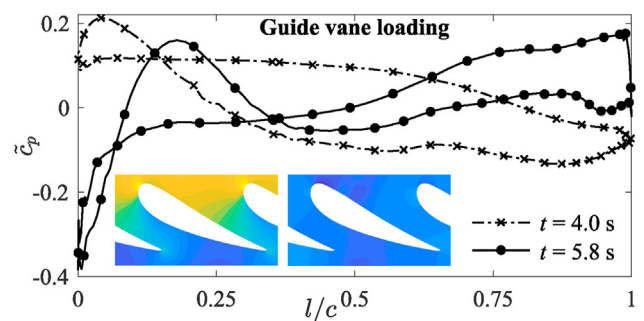
Fig. 9 shows pressure field in the vaneless space for non-cavitating ($t = 4$ s) and intense cavitating ($t = 5.8$ s) situations. To extract pressure values, a polyline (circle) along the runner

Fig. 6. Unsteady pressure fluctuations at k_1, k_2, and k_3 locations in the vaneless space. The locations are 120° circumferentially apart at same radius from the turbine axis.

Fig. 7. Coefficient of pressure at mid-span of the guide vane (#19) for non-cavitating ($t = 4$ s) and cavitating ($t = 5.8$ s) conditions. $l/c = 0$ and 1 indicate leading and trailing edges of the guide vane.

circumference is created, which passes through k_1, k_2 and k_3 points in the vaneless space (see Fig. 8 for the points). In the vaneless space, generally two distinct pressure fields are observed: (1) a rotating pressure field attached to the blade leading edge and (2) a stationary pressure field attached to the guide vane trailing edge. Fig. 9(a) shows fluctuations of combined pressure field for non-cavitating and regular operation of turbine. The angular position of θ on $x - axis$ is identical to that is shown in Fig. 8. The fluctuations are along the runner circumference $\theta = 0 - 360°$ at the time instant of 4 s. The fluctuations are periodic, and peak in each period indicates the stagnant pressure around the guide vane trailing edge. The valley indicates the pressure between two neighboring guide vanes. The large period of low frequency (red line) shows global circumferential variation of static pressure from the rotor stator interactions. Fig. 9(b) shows pressure field for the intense cavitation condition at the time instant 5.8 s along the polyline. Completely different pattern of pressure can be seen. The low pressure zone in the vaneless space is from 90° to 270°, and the spot of the intense

Fig. 5. Pressure fluctuations at a location k_1 in the vaneless space, and cavitation (vapour volume fraction) in guide vane passages at time instant $t = 5.8$ s.
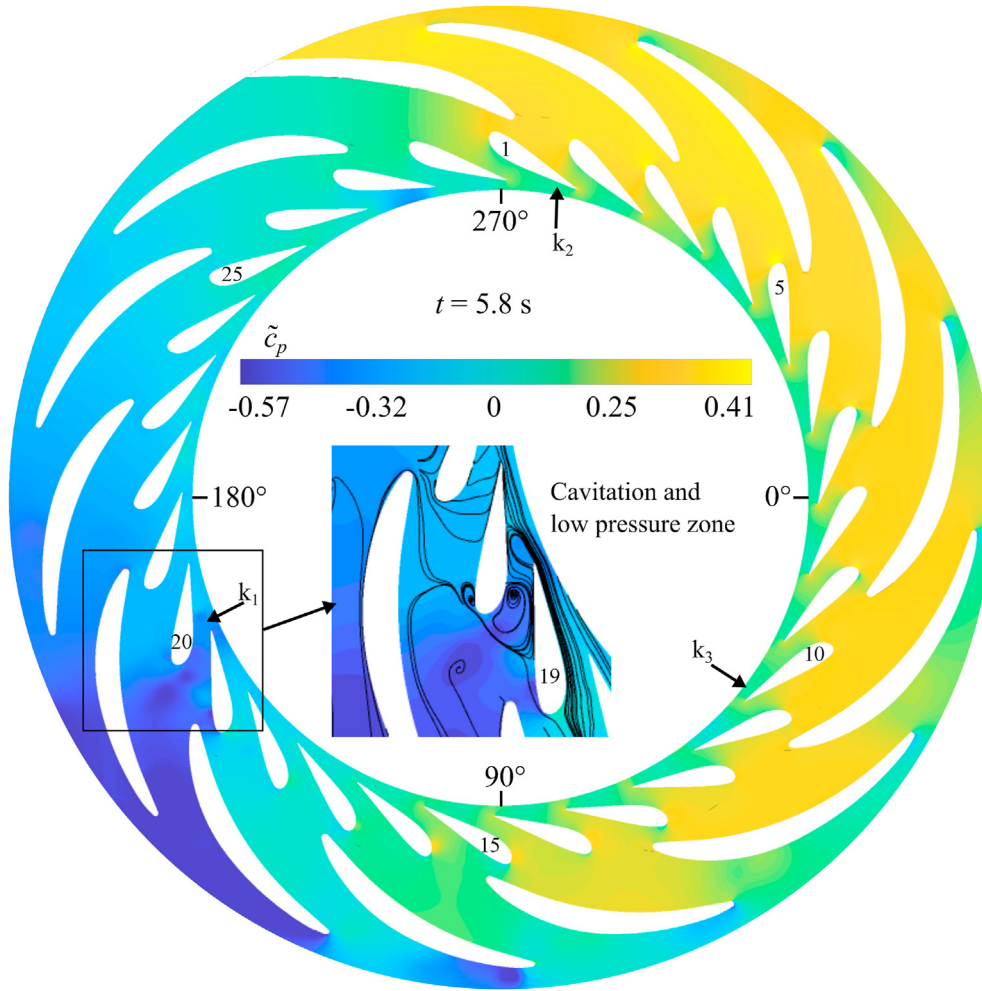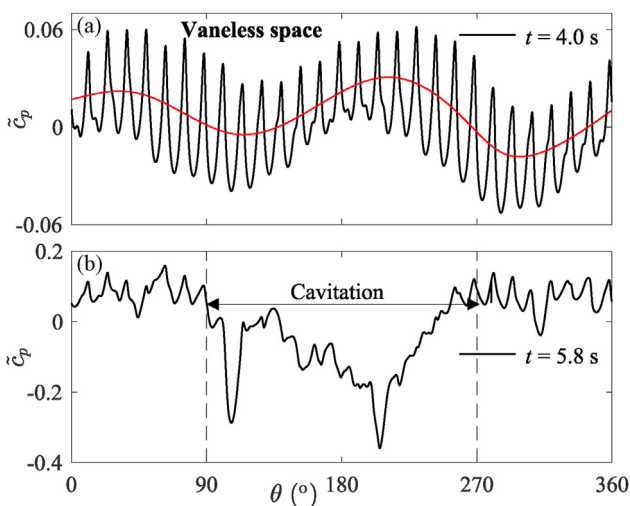
Fig. 8. Contours of coefficient of pressure in the guide vane and stay vane channels during intense cavitation ($t = 5.8$ s) in the turbine. k_1, k_2, and k_3 are pressure monitoring points in the vaneless space. The extended window around guide vane #20 shows the pressure contours superimposed by streamlines.

Fig. 9. Circumferential pressure along a polyline (circle) passing through k_1, k_2, and k_3 locations in the vaneless space for non-cavitating ($t = 4$ s) and cavitating ($t = 5.8$ s) conditions. Scale for y-axis is different to facilitate the clear visualization of fluctuations.

cavitation can be seen, where the coefficient of pressure, $\tilde{c}_p$, is

significantly low. Presence of cavitation has largely impacted the periodic variation of pressure, as presented Fig. 9(a). That means guide vane and the runner blade channels experience different pressure loading. The resulting blade loading along the blade span from-hub-to-shroud is asymmetric. This also indicates that, during cavitation condition, flow field associated with rotor-stator interaction may substantially differ from that of the normal rotor-stator interaction pattern. Such high intensity cavitation was also observed in the runner and draft tube at the same time. While analysing the pressure data and the occurrence of cavitation in the spiral casing, stay vanes and guide vanes, no specific pattern is found however, it appears that the cavitation is triggered from the runner.

Several numerical monitoring points were created (see Fig. 10) on the blade pressure side, suction side, leading edge and trailing edge to acquire unsteady pressure. The pressure on the blade during 4–7 s is shown in Fig. 11. Pressure fluctuations during 0–4 s are not shown in the figure because they are normal (no cavitation), and no significant change is seen, except increase of static pressure with rotational speed. The fluctuations are mainly related to the rotor-stator interaction, guide vane passing frequency (f_r).

$$f_r = n z_{gv} (\text{Hz}), \tag{6}$$

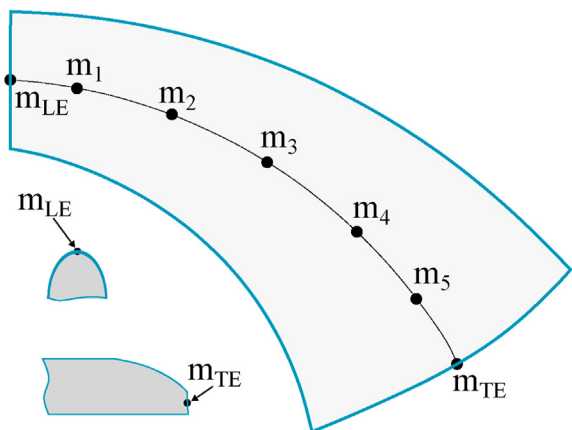where n is the runner rotational speed in revolutions per second

Fig. 10. Numerical monitoring points on the blade surface, pressure and suction sides.

and z_{gv} is the number of guide vanes. Unlike the conventional synchronous-speed turbine, the frequency, f_r in the present case is continuously changing with rotational speed of the runner. High-amplitude fluctuations related to the occurrence of cavitation and the resulting bubble collapse. The first instance of cavitation and the vapour pressure were observed around 4.6 s. Further investigating the pressure data around 4.8 s, it seems that front part of blade channel ($0 \leq l/c \leq 0.5$) is strongly affected by the cavitation, while the remaining half part ($l/c > 0.5$) experiences cavitation of low intensity or almost cavitation free. The high-amplitude pressure pulse was recorded at leading edge (m_{LE}), m_1 and m_2 locations. Flow field later appears to stable (cavitation free), and the next cavitation phase was recorded at 5.1–5.3 s, 5.7–6.2 s and 6.6–6.9 s. During the different phases of cavitation, intensity along the blade length varied significantly, and was dependent on the local pressure. For example, at 5.8 s, cavitation intensity was very high at all the locations while, around 6 s and 6.7 s, the cavitation intensity was reduced, especially m_5 and m_6 locations. Pressure signal m_{TE} (see Fig. 11(g)) shows low pressure all the time, which indicates the predominant presence of cavitation bubbles along the trailing edge. Time history of pressure along the trailing edge, from hub to shroud, is presented in Fig. 12. $t = 1 - 6$ s corresponds to variation of runner speed. The pressure fluctuations on the trailing edge are quite different from that of pressure/suctions side of the blade. Between 0 and 1 s, low frequency (≈ 5 Hz) fluctuations are predominant, which seem to be associated with the cavitation effect and the rotating pressure field at the runner outlet, high load vortex breakdown. Between 1 and 2, random occurrence of cavitation results in sudden pressure drop at the trailing edge. There is no systematic pattern, therefore it may be incorrect to associate with any phenomenon except change in load or the operating condition. No significant change in the pressure field was observed up to 4.6 s except random pulsations of low intensity cavitation near to shroud. Inception of cavitation for longer time was seen between 4.63 s and 4.85 s. Around 4.8 s, the bubble reaches to threshold condition and bursts, which induced high-amplitude pressure pulse at 4.82 s. The phases of cavitation inception can be seen in the extended Fig. 12(d) − (f). Cavitation intensity along the trailing edge points is different however, the maximum intensity is found on the points near to hub, i.e., m_{TE1} and m_{TE2}. Intensified cavitation and the repeated bubble bursts can be seen between 5.8 and 5.9 s. During this period, cavitation occurs in all channels of the runner and marginally expands to the vaneless space and the daft tube.

Analysis of pressure loading data on the blade revealed quite useful signature of wall attached cavitation. The blade loading at different spans and the cavitation condition is presented in Fig. 13.
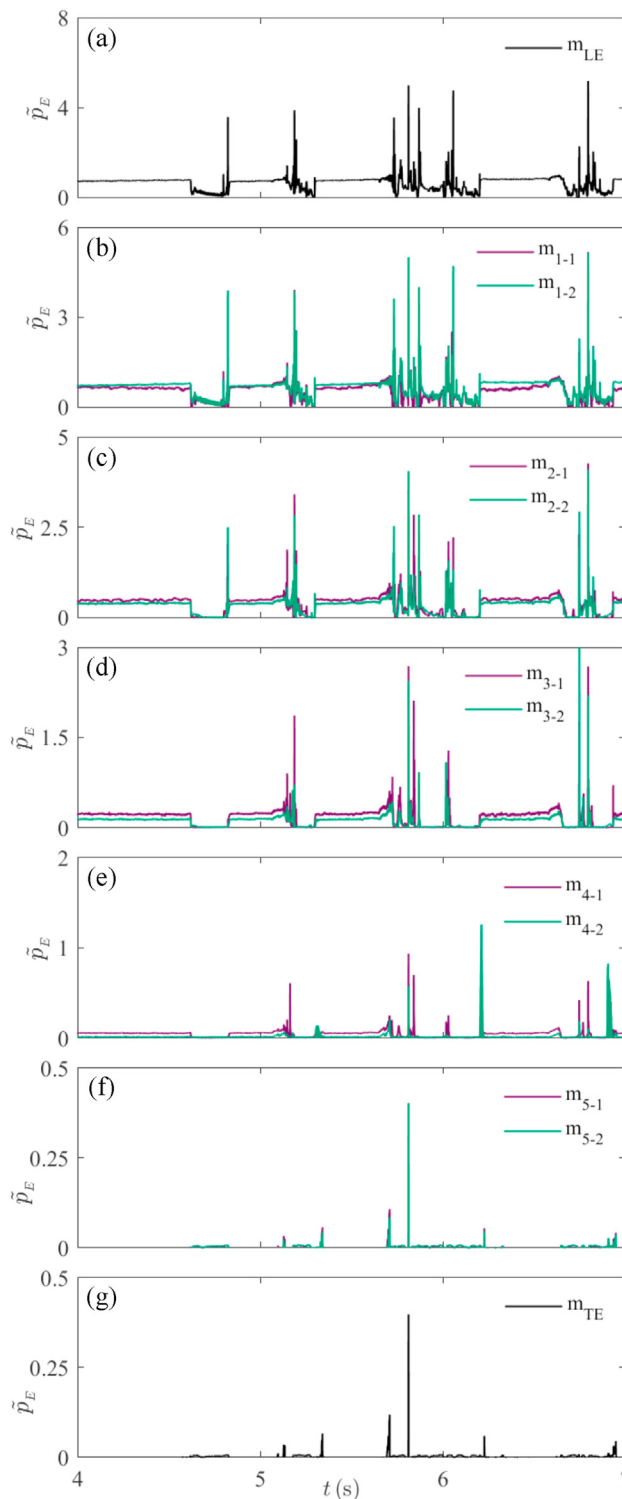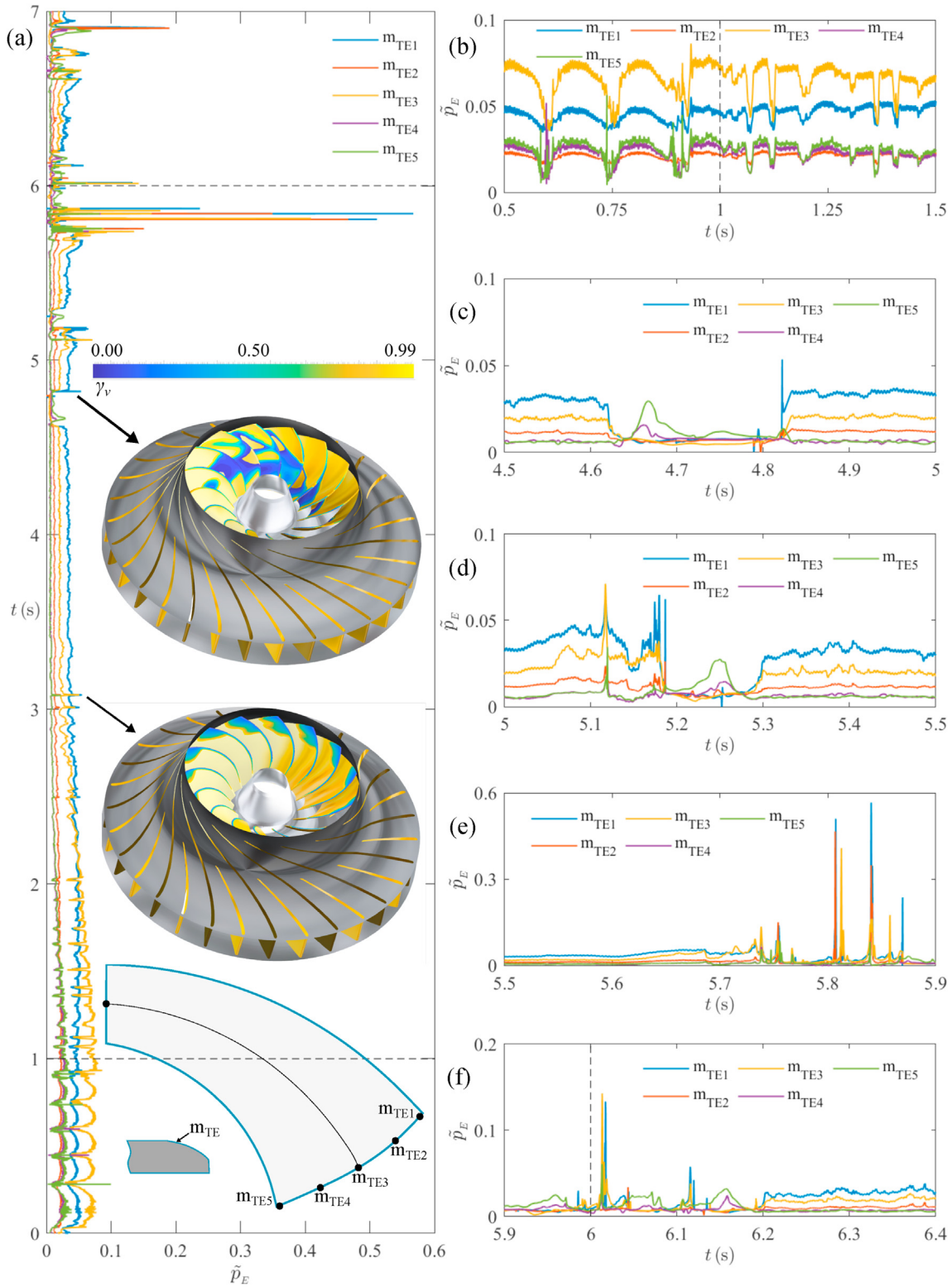

Fig. 11. Time history of pressure fluctuations on the blade surface. Locations of the numerical monitoring points are shown in Fig. 10. For example, m_{1-1} and m_{1-2} indicates (the point m_1) on the blade pressure and suction sides, respectively. Scale for $y - axis$ is different to facilitate the clear visualization of fluctuations.

The pressure loading ($\tilde{c}_p$) is normalized using net head (equation (5)), and represents the instantaneous static pressure on one blade (blade #14). During non-cavitating condition ($t = 4$ s), pressure loading across the span is symmetric — as expected — and gradually decreasing along the chord length. However, at 4.6 s (Fig. 13(b)), the

Fig. 12. Time history of pressure fluctuations at the blade trailing edge (m$_{TE}$) points. Figures (b)–(f) shows extended plots of figure (a) for more clarity on pressure loading. Scale for $y - axis$ is different to facilitate the clear visualization of fluctuations.

blade experienced vapour pressure on large part of the blade, and at certain locations, the cavitation spots were observed. At 4.8 s, sudden increase in pressure on the blade ($l/s = 0$ and $l/c = 0.8$) was appeared, which is result of burst of cavitation bubble. At 5.8 s, intense cavitation condition, pressure loading was unexpectedly

high (seven times the head). Then drops to very low (almost 2 kPa, below the vapour pressure), and resulted in intense cavitation at the runner outlet and around the trailing edge. Fig. 14 shows pressure and velocity variation along the blade channel during cavitating and non-cavitating conditions. Hub-to-shroud (spanwise) polylines were
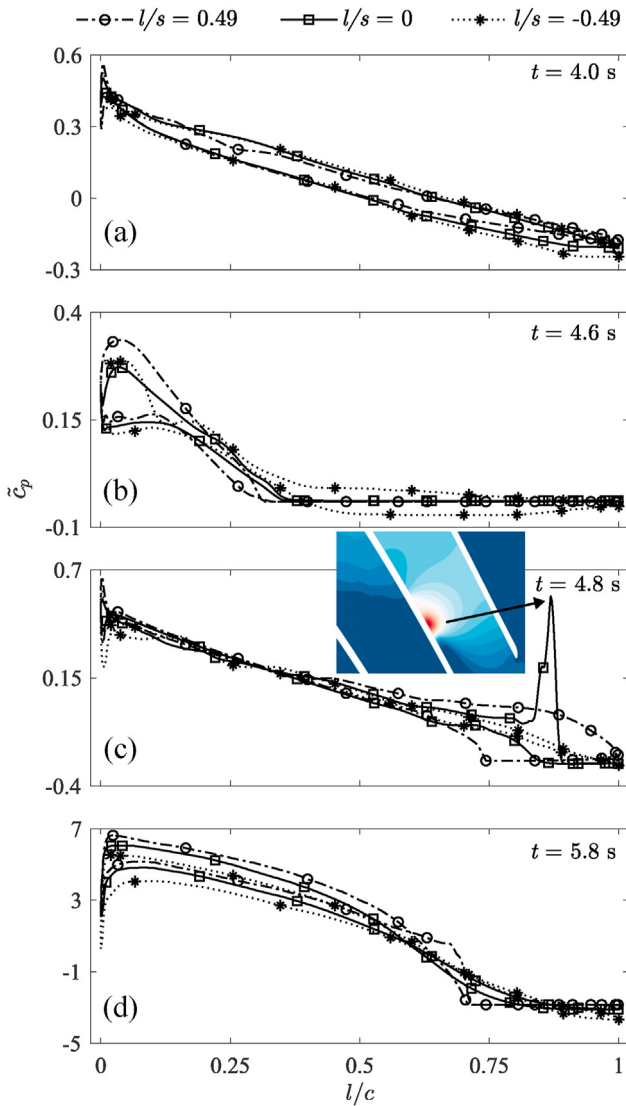
Fig. 13. Blade loading at different spans of the blade (Blade#14). On $x-$ axis, $l/c = 0$ and 1 indicate the blade leading and trailing edges, respectively. $l/s = 0.5$, 0 and -0.5 indicate the hub, blade mid-span and shroud, respectively. Scale for $y-$ axis is different to facilitate the clear visualization of loading.

created at 5, 25, 50, 75 and 95% of chord length (c) along the blade channel. The normalized values l/c of 0 and 1 represents the blade leading and trailing edges, respectively. On $y-$ axis, the normalized values l/s of 0.5, 0 and -0.5 represent the hub, mid-span and shroud, respectively. Three instances of time, i.e., 4, 4.8 and 5.8 s, are presented. Pressure values are normalized between 0 and 1 to extract the local profile (p^*). Time stamp $t = 4$ s is non-cavitating condition, and the pressure distribution is well within the expected range. Adverse pressure gradient at the span (l/s) 0.25−0.5, is the result of small swirling zone at the inlet of the blade channels. As rotational speed increases, inlet flow angle is skewed and causes separation from the leading edge towards the suction side. The separated flow creates small vortical region along the blade span. More about the inception of vortical region in the runner channels is presented in our previous work [52]. Pressure loading during the cavitating condition (5.8 s, Fig. 14(a)) is interestingly opposite to that of non-cavitating condition. Pressure loading at 25 and 50% of chord length (Fig. 14(b) and (c)) is normal for all three cases however, substantial variation can be seen at 75 and 95% of chord length

(Fig. 14(d) and (e)). Pressure from hub to mid-span is very low, and the cavitation is intense. While closely examining the intense cavitation condition (5.8 s), pressure at 95% chord length is extremely low, and large part of the channel is filled with vapour. Velocity distribution along these polylines is shown in Fig. 14(f) − (j). The flow is accelerating near the hub and shroud for non-cavitating condition while the flow is decelerating for the cavitating condition. Velocity at 25% chord for cavitating condition is very low at the mid-span, which is contrary to the other two cases. Flow velocity at 50% chord length is quite different for all three cases. Non-cavitating condition ($t = 4$ s) shows gradual increase of flow velocity towards the shroud, and the low-cavitating condition ($t = 4.8$ s) shows accelerating/decelerating flow. The intense cavitation condition ($t = 5.8$ s) shows opposite behavior to the non-cavitating condition, i.e., high velocity near to hub and low velocity near to shroud.

Contours of static pressure ($t = 5.8$ s) in the runner (mid-span, $l/s = 0$) are presented in Fig. 15, which shows low pressure zones at distinct locations in the blade channels. Swirling flow around these locations is predominant, and, interestingly, majority of channels show such low pressure zones. The pressure coefficient $\tilde{c}_p = -0.32$ indicates the pressure equals to the vapour pressure and the intense cavitation areas, especially L_1 and L_3 locations. While investigating the other time-step, it seems that the flow separation from the leading edge towards suction side induces low-pressure region. Pressure in this region quickly drops to the level of vapour pressure and develops a bubble, which attaches to the blade. In some cases, due to high velocity and steep curvature of blades, the bubble detaches from the wall, and later bursts. Fig. 16 shows pressure along the lines L_1, L_2, L_3 and L_3. On $x-$ axis, $\theta = 12°$ indicates the width of blade channel, e.g., $360°/30$ blades $= 12°$. We can see that the pressure coefficient at L_1 and L_3 is minimum indicating the vapour pressure zones in the channel. Pressure along the lines L_2, L_3 and L_3 indicates the different phases of occurrence of cavitation, where pressure drops from the normal condition (L_2) to the vapour phase (L_3). The velocity distribution along these lines is presented in Fig. 17. The velocity is normalized using equation (7).

$$v_c = \frac{|v|}{v_{th}}, \tag{7}$$

where $|v| = \sqrt{v_a^2 + v_r^2 + v_\omega^2}$ and $v_{th} = \sqrt{2gH}$; v_a, v_r and v_ω are axial, radial and circumferential velocities in m s^{-1}, respectively. L_1 shows high gradient of velocity due to the presence of vortical zone. Velocity on the blade suction side is high and reduces towards the middle of the channel (dead zone) then increases near to pressure side of the adjacent blade. In this region, $\theta = 8 - 11°$, of the blade channel flow is rapidly accelerating and gives momentum to the recirculating zone and drives downstream. While investigating the velocity for L_2, L_3 and L_3, no substantial deviation was observed, and the overall trend is similar, except minor variation in local velocity.

Flow at the runner outlet is generally chaotic and highly unsteady. Vortical flow leaving a blade channel interacts with the vortical flow of neighboring channel, and, at same time, vortex leaving the blade trailing edge also interacts [53]. This results in complex situation, where the stochastic type pressure fluctuations prevail. Furthermore, different flow velocity at the hub and shroud induces non-uniform distribution of flow in radial direction. During variable-speed operation, especially in this turbine, flow rate decreases as rotational speed increases, thus flow field changes constantly, and increase in rotational speed also induces more centrifugal force and the flow tends to move towards the shroud. Under steady state condition, cavitation is generally observed around the blade junctions to hub and shroud depending on turbine load. However, in some cases, the cavitation appears along the
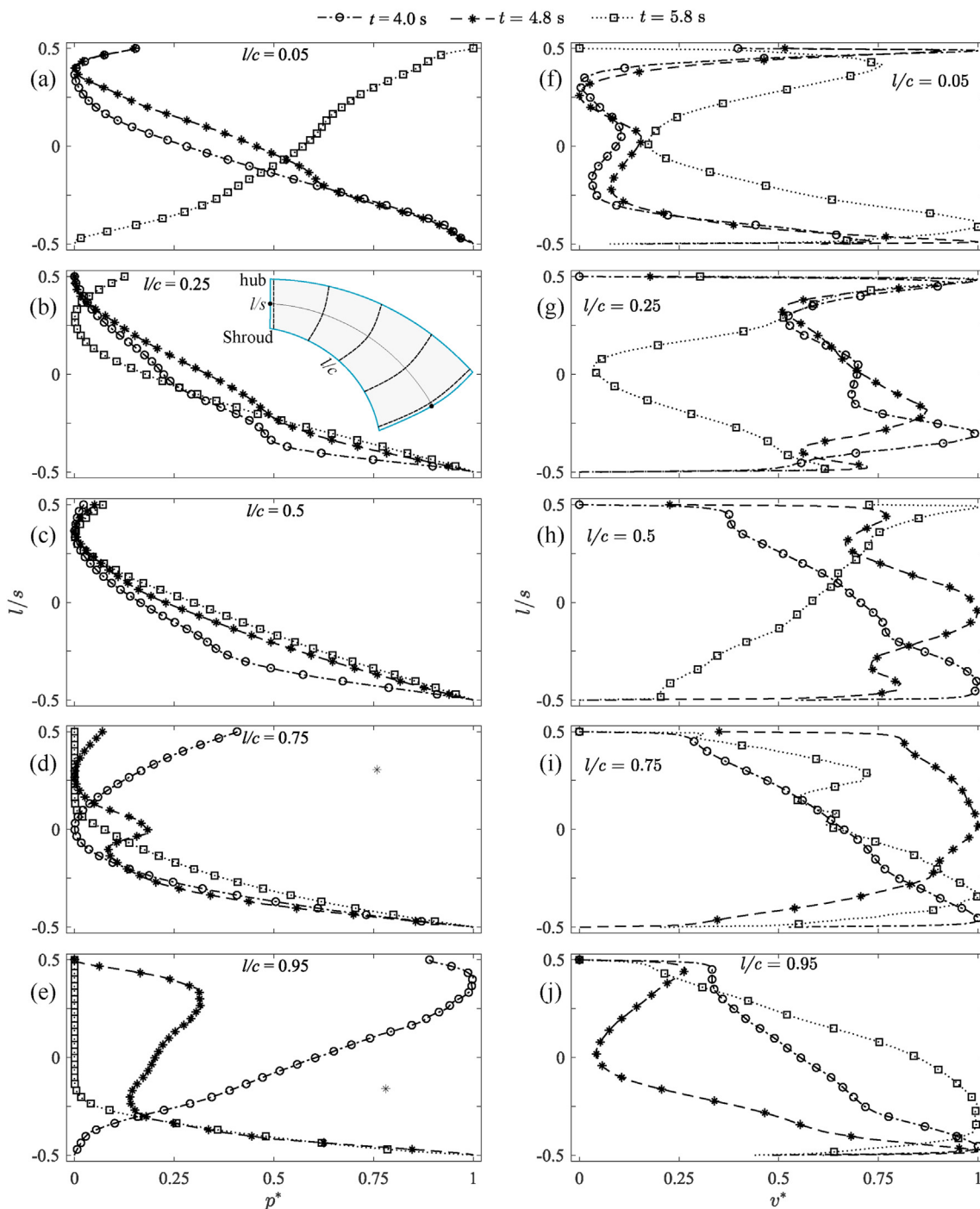
Fig. 14. Pressure and velocity variation hub-to-shroud along the blade length. On $y - axis$, $l/s = 0.5$, 0 and -0.5 indicate the hub, blade mid-span and shroud, respectively. $l/c = 0$ and 1 indicate the blade leading and trailing edges, respectively. $t = 4$ s is the non-cavitating condition, $t = 4.8$ and 5.8 s are the cavitating conditions.

entire span of trailing edge, i.e., from hub to shroud (see Fig. 12, $t = 3$ s). Four numerical monitoring points (k_3, k_5, k_6 and k_7) were created at the runner downstream. Monitored pressure signals are presented in Fig. 18 for the entire time series of simulation. Pressure variation in the draft tube is quite different from that of vaneless space and runner. Flow at these locations is highly chaotic and cavitating almost all the time. Time span of 0−1 s shows steady state operation, where rotational speed was constant. Fluctuations during this span are quite different, and the cavitation appears around k_6 and k_7 locations, $t = 0.5$ s. During speed variation, 1−6 s,

pressure amplitudes are random and the effect of localized cavitation from the bubble collapse is visible. After 4 s, pressure signal is almost steady indicating the vapour pressure and the location is surrounded by the vapour bubble attached on the draft tube wall. All monitoring points, $k_3 - k_7$, in the draft tube are covered by a large vapour ring/filament attached to the draft tube wall. The similar pattern is obtained at other time instances between 5 s and 7 s. The filament breaks up and causes high-amplitude pulse, which is visible between 5.1 s and 5.3 s. However, the intensity at these locations is different. Contours of vapour volume fraction at the
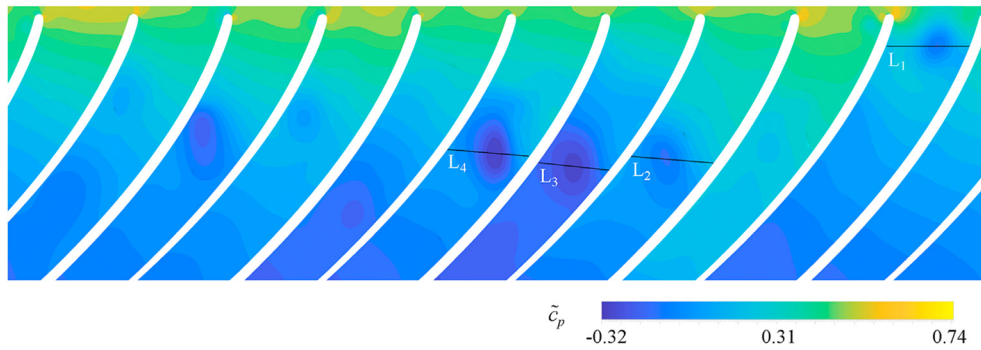
Fig. 15. Pressure contours on the runner mid-span ($l/s = 0$ and $t = 5.8$ s). L_1, L_2, L_3 and L_3 are lines used to extract pressure and velocity, which are presented in Figs. 17 and 18.
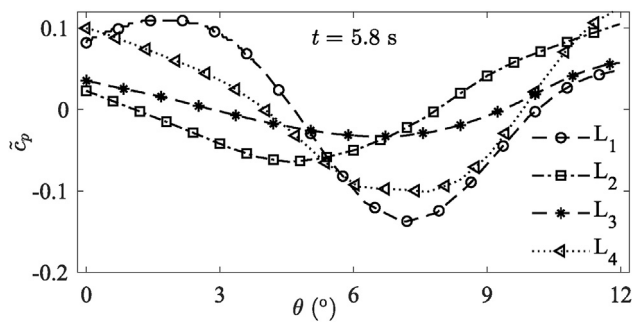

Fig. 16. Pressure along the lines L_1, L_2, L_3 and L_3 drawn in the runner channels from suction side to pressure side of neighboring blade. On $x-axis$: $\theta = 0°$ indicates the suction side of a blade and $\theta = 1°$ indicates pressure side of the adjacent blade of the channel.
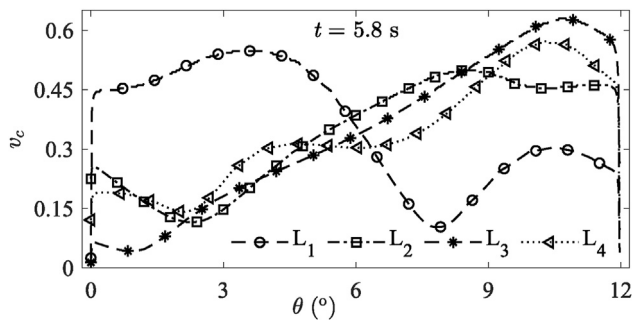

Fig. 17. Flow velocity along the lines L_1, L_2, L_3 and L_3 drawn in the runner channels from suction side to pressure side of neighboring blade. On $x-axis$: $\theta = 0°$ indicates the suction side of a blade and $\theta = 1°$ indicates pressure side of the adjacent blade of the channel.

same cross section as numerical monitoring point are shown in Fig. 19. The contours at time instances of 1, 3, 4 and 6 s are shown. At 1 s, vapour phase is concentrated into two regions, center core and mainstream core, however, near the wall, water phase is predominant. The interesting pattern can be seen 4 s, where the vapour and liquid phases are in complex share (kind of Nebula). The phases change quickly, vapour phase is present around k_3 and k_7 points, liquid phase is present around k_5 and k_6 points. Another Nebula type structure can be seen at 6 s, which induced high amplitude fluctuations, most likely collapsing of bubbles at high frequency near to monitoring points. Pressure and velocity contours at the same instances are presented in Figs. 20 and 21, respectively. Low pressure (vapour pressure) in the center core can be seen, and near to the wall, pressure is low, but the flow is non-cavitating. Around 6 s, in addition to the center core, another cavitating zone is established between k_5 and k_6 points, the pressure coefficient ($\tilde{c}_p$) is around -0.004. While investigating the velocity contours, quite interesting patterns are obtained, especially for $t = 4$ s. Velocity, where the liquid phase is predominant (see Fig. 19). In the other regions, the velocity is moderate, and the tiny recirculating regions are present, near to k_5 and k_7 points.

For conventional synchronous-speed turbine, at part load and high load operations, angle of flow velocity is highly skewed where flow outlet angle does not meet the blade inlet angle optimally, and the separation of flow from the leading edge is predominant. While using the speed variation option, circumferential velocity at the runner inlet can be optimized by optimizing the rotational speed and resulting flow separation from the blades is minimum. On the contrary to synchronous-speed turbines, while considering the variable-speed operation, consequences pertained to cavitating vortex breakdown can be reduced by optimizing the rotational speed and improving the flow angle with respect to circumferential velocity. However, the challenge is the mapping of cavitation characteristics along the speed variation. From the present study, it
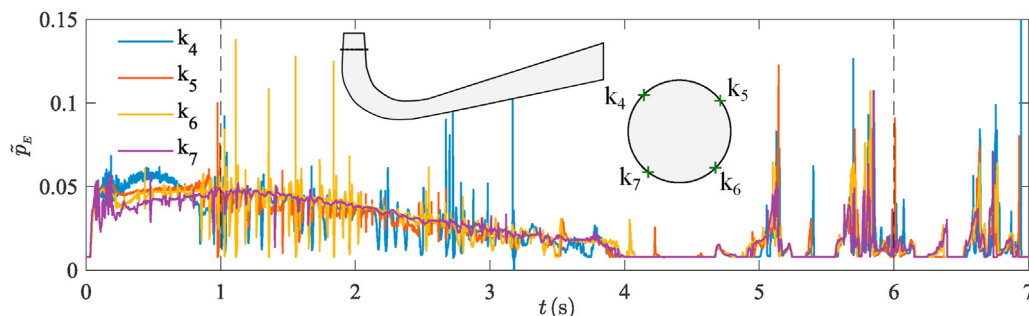

Fig. 18. Pressure fluctuations at runner downstream during speed-variation. k_3, k_5, k_6 and k_7 are the numerical monitoring points created on the wall of draft tube cone.
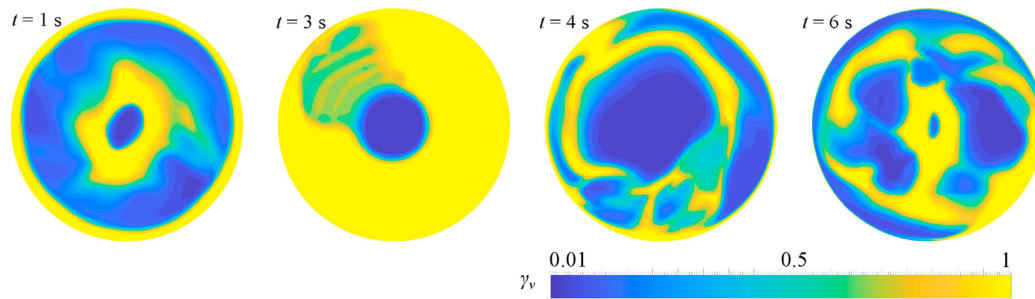
Fig. 19. Contours of vapour volume fraction in the draft tube, k_3, k_5, k_6 and k_7 cross section. $\gamma_v = 0$ and 1 indicate the vapour and liquid (water) phases, respectively.
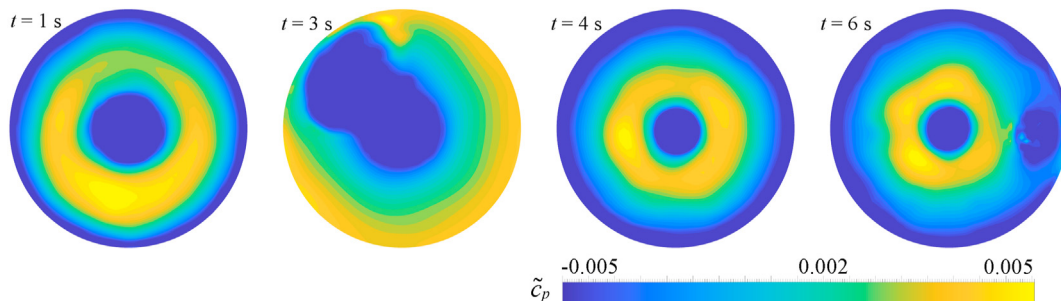

Fig. 20. Contours of pressure coefficient in the draft tube, k_3, k_5, k_6 and k_7 cross section.
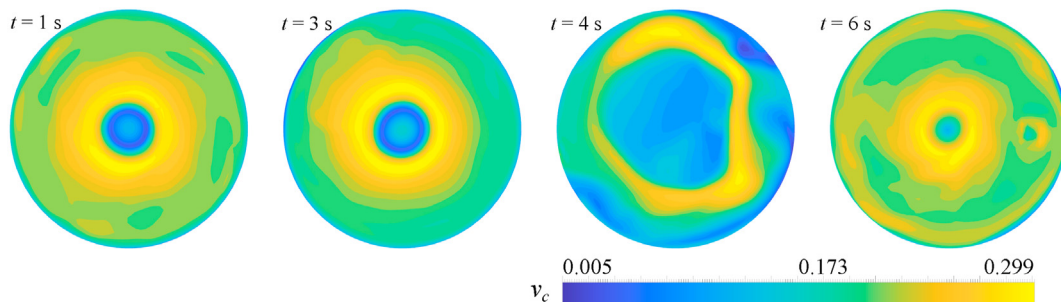

Fig. 21. Contours of velocity (v_c) in the draft tube, k_3, k_5, k_6 and k_7 cross section.

is clear that the cavitation occurs at certain time instants along the path of speed variation. Rotational speed where the cavitation is intense, can be avoided. It is worth to note—cavitation may be intense while crossing the threshold value of rotational speed, in this turbine 10% more than the synchronous speed. It is not possible to draw universal conclusion as the cavitation characteristics vary from one turbine to another. However, when we design a variable-speed turbine, additional challenge of intense cavitation may arise at certain points along the path of speed variation. This may case substantial damage to the turbine (although it may be momentarily), and the turbine may be restricted to operate in those regions. It is safe to carry out credible assessment of submergence level for variable-speed operation and to enforce extra factor of safety. That will be helpful to prevent the intense cavitation (similar to $t = 5.8$ s in this turbine) and strong fluctuations in the power output.

4. Conclusions

The extreme operation condition was considered for the present study that allows to simulate the worst cavitation situation in a turbine. For variable-speed operation, the prediction of cavitation is challenging due to change of rotational speed and the momentary occurrence of transient phenomena. The study showed specific instances of cavitation, where the large part of the turbine was cavitating intensely, including stay vane and guide vane passages. During the initial phase of speed variation, small cavitation spots at the trailing edge junction near to hub and shroud were obtained. The cavitation was automatically disappeared as rotational speed increased further, however, at high rotational speed ($n/n_{ED} > 1.1$), the cavitation was maximum. Some of the blade and guide vane channels were filled with vapour content. Fluctuations in torque were high because energy extracted by the blades was asymmetric. Some of the blade channels experiences intense cavitation while others were performing normal. Study on blade loading in the cavitating channels revealed quite interesting pattern, certain part of the channel seems to pumping (higher pressure on the suction side and lower pressure on pressure side) where the cavitation is predominant while the other section was normal. From the present work, it appears that the cavitation become intense while crossing the threshold value of rotational speed. In this turbine, the threshold value is 10% of the synchronous speed.

5. Further work

- Further work will aim to investigate the mechanics of cavitation bubble inception and collapse on the walls of the blades with fine mesh ($y^+ \leq 1$) — large eddy simulation.
- The present simulations consumed around one million cpu hours on supercomputer. The effort will be made to reduce the computational domain, modeling of runner passage only, and use existing computational model to impose transient boundary conditions.

Funding

Declaration of competing interest

The authors declare that they have no known competing financial interests or personal relationships that could have appeared to influence the work reported in this paper.

References

[1] H. Keck, T. Weiss, W. Michler, M. Sick, Recent developments in the dynamic analysis of water turbines, Proc. IME J. Power Energy 223 (2009) 415—427, https://doi.org/10.1243/09576509JPE578.

[2] X. Liu, Y. Luo, Z. Wang, A review on fatigue damage mechanism in hydro turbines, Renew. Sustain. Energy Rev. 54 (2016) 1—14, https://doi.org/10.1016/j.rser.2015.09.025.

[3] C. Trivedi, M.J. Cervantes, Fluid structure interaction in hydraulic turbines: a perspective review, Renew. Sustain. Energy Rev. 68 (2017) 87—101, https://doi.org/10.1016/j.rser.2016.09.121.

[4] I. Iliev, C. Trivedi, O.G. Dahlhaug, Variable-speed operation of Francis turbines: a review of the perspectives and challenges, Renew. Sustain. Energy Rev. 103 (2019) 109—121, https://doi.org/10.1016/j.rser.2018.12.033.

[5] C. Trivedi, E. Agnalt, O.G. Dahlhaug, Investigations of unsteady pressure loading in a Francis turbine during variable-speed operation, Renew. Energy 113 (2017) 397—410, https://doi.org/10.1016/j.renene.2017.06.005.

[6] C. Trivedi, E. Agnalt, O.G. Dahlhaug, Experimental study of a Francis turbine under variable-speed and discharge conditions, Renew. Energy 119 (2018) 447—458, https://doi.org/10.1016/j.renene.2017.12.040.

[7] J.L. Gordon, Hydraulic turbine efficiency, Can. J. Civ. Eng. 28 (2001) 238—253, https://doi.org/10.1139/l00-102.

[8] P.P. Gohil, R.P. Saini, Coalesced effect of cavitation and silt erosion in hydro turbines-A review, Renew. Sustain. Energy Rev. 33 (2014) 280—289, https://doi.org/10.1016/j.rser.2014.01.075.

[9] X.-w. Luo, B. Ji, Y. Tsujimoto, A review of cavitation in hydraulic machinery, Journal of Hydrodynamics, Ser. B 28 (2016) 335—358, https://doi.org/10.1016/S1001-6058(16)60638-8.

[10] J.-P. Franc, J.-M. Michel, Fundamentals of Cavitation, Fluid Mechanics and its Applications, Springer Netherlands, Dordrecht, The Netherlands, 2005, https://doi.org/10.1007/1-4020-2233-6. URL.

[11] X. Escaler, E. Egusquiza, M. Farhat, F. Avellan, M. Coussirat, Detection of cavitation in hydraulic turbines, Mech. Syst. Signal Process. 20 (2006) 983—1007, https://doi.org/10.1016/j.ymssp.2004.08.006.

[12] X. Escaler, J.V. Ekanger, H.H. Francke, M. Kjeldsen, T.K. Nielsen, Detection of draft tube surge and erosive blade cavitation in a full-scale Francis turbine, J. Fluid Eng. 137 (2015), 011103—9, https://doi.org/10.1115/1.4027541.

[13] A. Favrel, J. Gomes, C. Landry, A. Muller, C. Nicolet, F. Avellan, New insight in Francis turbine cavitation vortex rope: role of the runner outlet flow swirl number, J. Hydraul. Res. 56 (2018) 367—379, https://doi.org/10.1080/00221686.2017.1356758.

[14] L. Chen, L. Zhang, X. Peng, X. Shao, Influence of water quality on the tip vortex cavitation inception, Phys. Fluids 31 (2019), 023303—13, https://doi.org/10.1063/1.5053930.

[15] V.H. Arakeri, Viscous effects on the position of cavitation separation from smooth bodies, J. Fluid Mech. 68 (1975) 779—799, https://doi.org/10.1017/S0022112075001231.

[16] P. Ausoni, A. Zobeiri, F. Avellan, M. Farhat, The effects of a tripped turbulent boundary layer on vortex shedding from a blunt trailing edge hydrofoil, J. Fluid Eng. 134 (2012), 051207—11, https://doi.org/10.1115/1.4006700.

[17] P.F. Pelz, T. Keil, T.F. Grob, The transition from sheet to cloud cavitation, J. Fluid Mech. 817 (2017) 439—454, https://doi.org/10.1017/jfm.2017.75.

[18] Z. Zuo, S. Liu, D. Liu, D. Qin, Y. Wu, Numerical predictions of the incipient and developed interblade vortex lines of a model Francis turbine by cavitation calculations, Adv. Mech. Eng. 5 (2013) 1—7, https://doi.org/10.1155/2013/397583.

[19] K. Yamamoto, A. Muller, A. Favrel, F. Avellan, Experimental evidence of inter-blade cavitation vortex development in Francis turbines at deep part load condition, Exp. Fluid 58 (2017), 142—14, https://doi.org/10.1007/s00348-017-2421-z.

[20] L.A. Teran, S.A. Rodriguez, S. Lain, S. Jung, Interaction of particles with a cavitation bubble near a solid wall, Phys. Fluids 30 (2018) 123304—123312, https://doi.org/10.1063/1.5063472.

[21] B. Boyd, S. Becker, Numerical modeling of the acoustically driven growth and collapse of a cavitation bubble near a wall, Phys. Fluids 31 (2019), 032102—20, https://doi.org/10.1063/1.5084729.

[22] T. Du, Y. Wang, L. Liao, C. Huang, A numerical model for the evolution of internal structure of cavitation cloud, Phys. Fluids 28 (2016), 077103—19, https://doi.org/10.1063/1.4958885.

[23] F. Avellan, Introduction to cavitation in hydraulic machinery. Scientific Bulletin of the Politehnica University of Timisoara Transactions on Mechanics, Special Issue, Politehnica University of Timisoara, Timisoara, Romania, 2004, p. 14.

[24] IEC 60193, Hydraulic turbines, storage pumps and pump-turbines: model acceptance tests, in: Tech. rep., International Electrotechnical Commission, vol. 3, 1999 rue de VarembÃ©, PO Box 131, CH-1211 Geneva 20, Switzerland, 16 November.

[25] S. Liu, L. Zhang, M. Nishi, Y. Wu, Cavitating turbulent flow simulation in a Francis turbine based on mixture model, J. Fluid Eng. 131 (2009), 051302—8, https://doi.org/10.1115/1.3112382.

[26] A. Muller, M. Dreyer, N. Andreini, F. Avellan, Draft tube discharge fluctuation during self-sustained pressure surge: fluorescent particle image velocimetry in two-phase flow, Exp. Fluid 54 (2013), 1514—11, https://doi.org/10.1007/s00348-013-1514-6.

[27] R. Tao, R. Xiao, F. Wang, W. Liu, Improving the cavitation inception performance of a reversible pump-turbine in pump mode by blade profile redesign: design concept, method and applications, Renew. Energy 133 (2019) 325—342, https://doi.org/10.1016/j.renene.2018.09.108.

[28] A. Favrel, J. Gomes Pereira Junior, C. Landry, A. Muller, K. Yamaishi, F. Avellan, Dynamic modal analysis during reduced scale model tests of hydraulic turbines for hydro-acoustic characterization of cavitation flows, Mech. Syst. Signal Process. 117 (2019) 81—96, https://doi.org/10.1016/j.ymssp.2018.07.053.

[29] S.C. Roy, J.-P. Franc, M. Fivel, Cavitation erosion: using the target material as a pressure sensor, J. Appl. Phys. 118 (2015) 164905—164911, https://doi.org/10.1063/1.4934747.

[30] B. Ji, X. Luo, Y. Wu, X. Peng, Y. Duan, Numerical analysis of unsteady cavitating turbulent flow and shedding horse-shoe vortex structure around a twisted hydrofoil, Int. J. Multiphas. Flow 51 (2013) 33—43, https://doi.org/10.1016/j.ijmultiphaseflow.2012.11.008.

[31] D.T. Akcabay, E.J. Chae, Y.L. Young, A. Ducoin, J.A. Astolfi, Cavity induced vibration of flexible hydrofoils, J. Fluid Struct. 49 (2014) 463—484, https://doi.org/10.1016/j.jfluidstructs.2014.05.007.

[32] A. Favrel, A. Muller, C. Landry, K. Yamamoto, F. Avellan, LDV survey of cavitation and resonance effect on the precessing vortex rope dynamics in the draft tube of Francis turbines, Exp. Fluid 57 (2016), 168—16, https://doi.org/10.1007/s00348-016-2257-y.

[33] T. Cencic, M. Hocevar, B. Sirok, Study of erosive cavitation detection in pump mode of pump-storage hydropower plant prototype, J. Fluid Eng. 136 (2014), 051301—11, https://doi.org/10.1115/1.4026476.

[34] P. Ausoni, M. Farhat, X. Escaler, E. Egusquiza, F. Avellan, Cavitation influence on von karman vortex shedding and induced hydrofoil vibrations, J. Fluid Eng. 129 (2007) 966—973, https://doi.org/10.1115/1.2746907.

[35] N.A. Chang, J. Choi, R. Yakushiji, S.L. Ceccio, Cavitation inception during the interaction of a pair of counter-rotating vortices, Phys. Fluids 24 (2012), 014107, https://doi.org/10.1063/1.3674299.

[36] O.D.L. Torre, X. Escaler, E. Egusquiza, M. Farhat, Experimental investigation of added mass effects on a hydrofoil under cavitation conditions, J. Fluid Struct. 39 (2013) 173—187, https://doi.org/10.1016/j.jfluidstructs.2013.01.008.

[37] M. Dreyer, J. Decaix, C. Munch-Alligne, M. Farhat, Mind the gap: a new insight into the tip leakage vortex using stereo-PIV, Exp. Fluid 55 (2014) 1—13, https://doi.org/10.1007/s00348-014-1849-7.

[38] S. Pasche, F. Gallaire, M. Dreyer, M. Farhat, Obstacle-induced spiral vortex breakdown, Exp. Fluid 55 (2014) 1784, https://doi.org/10.1007/s00348-014-1784-7.

[39] E.L. Amromin, Design approach for cavitation tolerant hydrofoils and blades, J. Fluid Struct. 45 (2014) 96—106, https://doi.org/10.1016/j.jfluidstructs.2013.11.014.

[40] X. Liu, L. Zhou, X. Escaler, Z. Wang, Y. Luo, O. De La Torre, Numerical simulation of added mass effects on a hydrofoil in cavitating flow using acoustic Fluid-Structure Interaction, J. Fluid Eng. 139 (2017), 041301—8, https://doi.org/10.1115/1.4035113.

[41] H.-C. Yeh, W.-J. Yang, Dynamics of bubbles moving in liquids with pressure gradient, J. Appl. Phys. 39 (1968) 3156–3165, https://doi.org/10.1063/1.1656750.

[42] A. Ducoin, J.A. Astolfi, F. Deniset, J.-F. Sigrist, Computational and experimental investigation of flow over a transient pitching hydrofoil, Eur. J. Mech. B Fluid 28 (2009) 728–743, https://doi.org/10.1016/j.euromechflu.2009.06.001.

[43] B. Huang, A. Ducoin, Y.L. Young, Physical and numerical investigation of cavitating flows around a pitching hydrofoil, Phys. Fluids 25 (2013) 102109–102127, https://doi.org/10.1063/1.4825156.

[44] X.C. Wu, Y.W. Wang, C.G. Huang, Effect of mesh resolution on large eddy simulation of cloud cavitating flow around a three dimensional twisted hydrofoil, Eur. J. Mech. B Fluid 55 (2016) 229–240, https://doi.org/10.1016/j.euromechflu.2015.09.011.

[45] F.R. Menter, Review of the shear-stress transport turbulence model experience from an industrial perspective, Int. J. Comput. Fluid Dynam. 23 (2009) 305–316, https://doi.org/10.1080/10618560902773387.

[46] M.S. Plesset, The dynamics of cavitation bubbles, J. Appl. Mech. 16 (1949) 277–282.

[47] H. Cheng, X. Bai, X. Long, B. Ji, X. Peng, M. Farhat, Large eddy simulation of the tip-leakage cavitating flow with an insight on how cavitation influences vorticity and turbulence, Appl. Math. Model. 77 (2020) 788–809, https://doi.org/10.1016/j.apm.2019.08.005.

[48] C. Trivedi, A systematic validation of a Francis turbine under design and off-design loads, Journal of Verification, Validation and Uncertainty Quantification 4 (2019), 011003–16, https://doi.org/10.1115/1.4043965.

[49] AIAA G-077-1998, Guide for the Verification and Validation of Computational Fluid Dynamics Simulations, AIAA, Reston, VA, USA, 1998, https://doi.org/10.2514/4.472855.001. Tech. Rep. 1563472856.

[50] C. Trivedi, M.J. Cervantes, O.G. Dahlhaug, Numerical techniques applied to hydraulic turbines: a perspective review, Appl. Mech. Rev. 68 (2016), 010802–11, https://doi.org/10.1115/1.4032681.

[51] C. Trivedi, Investigations of compressible turbulent flow in a high head Francis turbine, J. Fluid Eng. 140 (2018), 011101–17, https://doi.org/10.1115/1.4037500.

[52] C. Trivedi, O.G. Dahlhaug, Interaction between trailing edge wake and vortex rings in a Francis turbine at runaway condition: compressible large eddy simulation, Phys. Fluids 30 (2018), 075101–15, https://doi.org/10.1063/1.5030867.

[53] C. Trivedi, Time-dependent inception of vortex rings in a Francis turbine during load variation: large eddy simulation and experimental validation, J. Hydraul. Res. 58 (2020) 790–806, https://doi.org/10.1080/00221686.2019.1671514.